Journal of Catalysis **203,** 7–17 (2001)
doi:10.1006/jcat.2001.3299, available online at http://www.idealibrary.com on IDEAL®

Nature of the Metal–Support Interaction in Supported Pt Catalysts: Shift in Pt Valence Orbital Energy and Charge Rearrangement

D. E. Ramaker,* J. de Graaf,† J. A. R. van Veen,‡ and D. C. Koningsberger†,[1]

*Chemistry Department, George Washington University, Washington, DC 20052; †Department of Inorganic Chemistry and Catalysis, Debye Institute, Utrecht University, P.O. Box 80083, 3508 TB Utrecht, The Netherlands; and ‡Shell International Chemicals B.V., Badhuisweg 3, 1031 CM Amsterdam, The Netherlands

Received September 28, 2000; revised February 21, 2001; accepted May 31, 2001; published online August 28, 2001

Conversion of neopentane (hydrogenolysis and isomerization on Pt/LTL, Pt/SiO_2–Al_2O_3, Pt/MgO–Al_2O_3) and tetralin (hydrogenation on Pt/Y) catalytic data, combined with spectroscopic Pt atomic XAFS (AXAFS) data, and theoretical calculations are utilized to elucidate the nature of the metal–support interaction for Pt-supported catalysts. The turnover frequency (TOF) of both the neopentane and tetralin conversion strongly depends on the composition of the support. The TOF increases with increasing acidity, polarization power of the charge-compensating cations (Na^+, H^+, K^+, La^{3+}), Si/Al ratio, and the presence of extra-framework Al. The intensity of the experimental Pt atomic XAFS correlates with the TOF. *Ab initio* scattered wave cluster calculations on a Pt_4O_3 cluster were performed using the FEFF7 code. The electron charge on the three "support" oxygens was changed from +0.05 to −0.01 electron to mimic changes in the support Madelung potential, which for the cluster is dominated by the nearest neighbor oxygen charge. The trends found in these theoretical AXAFS results are in excellent agreement with the experimental Pt AXAFS data and suggest that a metal cluster–support potential model is adequate for describing the changes seen in the experimental AXAFS. The experimental AXAFS results can also be understood using a molecular orbital scheme. This molecular orbital scheme further indicates that the metal–support interaction not only changes the ionization potential of the Pt valence orbitals but also induces a charge rearrangement from the Pt 6*s* orbitals within the particle to the oxygens of the Pt-support interface and vice versa. This charge rearrangement is also indicated by the AXAFS through the shift, ΔR, in AXAFS peak position. Both effects influence the electronic structure of the Pt particles. The changes in the electronic structure alter the catalytic properties of the Pt surface atoms by varying the bond strength and bond order (single or bridged) to the catalytic intermediates. The consequences of the metal–support interaction for tailor-made supported metal catalysts will be discussed. © 2001 Academic Press

Key Words: **Pt/NaY; Pt/H–USY; Pt/SiO_2–Al_2O_3; Pt/MgO–Al_2O_3; TOF of neopentane and tetralin conversion; metal–support interaction; sulfur tolerance; tailor-made supported metal catalysts; charge rearrangement; interatomic potential model; molecular orbital density of states diagram.**

INTRODUCTION

The metal–support interaction of supported metal catalysts has been shown to alter the catalytic behaviour but there are also indications in the literature that it changes the electronic properties of the supported metal cluster. Several explanations for the metal–support interaction have been proposed: (i) Formation of a metal–proton adduct, with the number of protons determined by the acidity of the support (1, 2), (ii) charge transfer between the metal atoms and the nearest neighbour zeolite oxygen atoms (3–5), and (iii) polarisation of the metal particles by nearby cations in the support (6, 7). It has been recently indicated (8) that most of these explanations are not based upon firm experimental ground and indeed some explanations contradict recent experimental data. Mojet *et al.* (9–11) have shown that the catalytic activity and spectroscopic properties of supported noble metal particles are greatly affected by the charge-compensating cations (H^+, K^+) in LTL zeolite and by the acidity/alkalinity of a mesoporous flat support (SiO_2). As the K^+ content of the support increases, the turnover frequency (TOF) of the metal particles for neopentane conversion decreases. At the same time, there is a decrease in the Pd XPS binding energy and a decrease in the linear to bridge bonded CO ratio for CO on Pd and Pt as revealed in the FTIR spectra. The XPS and the FTIR results give a strong indication for a direct influence of the support on the electronic properties of the metal particles. These effects were found to be independent of the type of the metal (Pd or Pt). The turnover frequency for the conversion of neopentane was also determined for Pt in Y zeolite with different numbers of protons and La^{3+} ions, different Si/Al ratios, and non-framework Al present (8). As in Pt/LTL, the Pt TOF was found to increase with the number of protons. The TOF of Pt in nonacidic NaLaY zeolite is about 25 times higher than that in NaY, which indicates that the charge of the cations has a strong influence on the TOF of Pt. A factor of 20 increase in the Pt TOF for K–USY compared to that for NaY is attributed to the effect of a higher Si/Al ratio and/or the presence of non-framework Al in the K–USY.

[1] To whom correspondence should be addressed. Fax: +(31) 30 2511027. E-mail: d.c.koningsberger@chem.uu.nl.

0021-9517/01 $35.00

Recently, we developed two new tools for obtaining electronic structural information from X-ray absorption fine structure (XAFS) data of metal-supported catalysts (12, 13). A previously nonutilized feature called atomic XAFS (AXAFS) has been shown to be highly sensitive to the composition of the support. The intensity of the AXAFS peak in the Fourier transform of the XAFS data increases with decreasing K/Al ratio for Pt/LTL (11). The intensity of the AXAFS peak in the Fourier transform of Pt/H–USY is also higher than that for Pt/NaY. The change in intensity of the Fourier transform AXAFS peak can be directly related to a change in interatomic potential of the Pt atoms averaged over the whole Pt metal particle. EXAFS has shown that the Pt metal particles are in direct contact with the support oxygen atoms. The change in interatomic potential is caused by a change in electron charge (more or less electron rich) of the support oxygen atoms. The electron charge of the support oxygen atoms in turn is determined by the Madelung potential of the support, which depends on the composition of the support. For the LTL support the electron charge (electron richness) decreases with decreasing K/Al ratio (11). For the Y support the replacement of Na^+ ions by protons, the higher Si/Al ratio, and/or the presence of framework Al in H–USY also decreases the electron richness of the support oxygen atoms (8). Further, a Pt–H antibonding shape resonance has been observed in the Pt L_2 and L_3 near-edge X-ray absorption spectra. The Pt–H antibonding state resonance is found to change with decreasing electron charge on the support oxygens for the same catalytic systems (8, 13–15). These results imply a change in the Pt–H bonding with a decrease in electron charge (decreasing electron richness) of the support oxygen atoms. Combining the XPS and CO FTIR results with the AXAFS and shape resonance data clearly shows that the metal–support interaction can be attributed primarily to a change in the energy position of the metal valence *d* orbitals interacting with the adsorbates (8, 13–15).

The combination of the results of the new spectroscopic tools (AXAFS and Pt–H shape resonance) with the catalytic data for neopentane conversion have thus led to new insights, on a molecular scale, concerning the essence of the metal–support interaction. So far, our work (8, 13–15) has established this for only one type of catalytic reaction (hydrogenolysis/isomerization) and only one aspect of this interaction, namely, a shift in the ionization potential of the valence orbital electrons. In a recent study (18, 19) we showed that the activity of Pt/NaY, Pt/NaLaY, Pt/NaH–USY, and Pt/H–USY for the hydrogenation of tetralin also depends on the composition of these zeolite supports. The process conditions (at 350°C in 60 bar hydrogen with 165 parts per million weight (ppmw) debezothiofene added to the feed) are comparable to industrial conditions for deep hydrotreatment of diesel.

In this work, we will use these catalytic results in an industrial highly important application to further elucidate the nature of the metal–support interaction in supported Pt catalysts. The consequences of the metal–support interaction for preparing tailor-made catalysts will be discussed. Results of analysis of experimental atomic XAFS data for Pt particles supported on zeolitic (LTL,Y) and amorphous mesoporous supports (SiO_2–Al_2O_3, MgO–Al_2O_3) will be summarized. These results will be compared with atomic XAFS data, which are obtained with *ab initio* multiple scattered wave calculations using the FEFF7 code on a Pt_4O_3 cluster. The results of these FEFF7 AXAFS calculations, previously published molecular orbital calculations, and group theory arguments on a highly symmetric Pt_4O_3 cluster make it possible to predict the MO mixing of Pt 6*s* and O $2p_z$ orbitals. These results clarify that the metal–support interaction also induces a charge rearrangement from the particle to or from the metal–support interface. The implications of this change in the electronic structure of the Pt particles on their catalytic behavior will be discussed.

EXPERIMENTAL

Details about the preparation of the catalysts, composition of the supports, neopentane conversion, and XAFS data collection are given elsewhere: for Pt/LTL, (11); for Pt/SiO_2–Al_2O_3 and Pt/MgO–Al_2O_3, (16).

Preparation of the Pt/Y Catalysts

These catalysts were prepared by ion exchange of supports with an aqueous solution of $Pt(NH_3)_4(NO_3)_2$ (Aldrich 27,872-6 p.a.). Commercial NaY (LZY 54), $NaNH_4$–USY (LZY 74), and NH_4–USY (LZY 84) zeolite powders without binder from UOP were used as supports. The support composition is given in Table 1. The catalysts were calcined at 300°C. A low heating rate of 0.2°C/min was necessary to obtain highly dispersed Pt particles with a narrow particle size distribution (17). XRD, hydrogen chemisorption, TEM, EXAFS, and Pt particle modeling were used to determine the Pt dispersion, (average) Pt particle size, and size distribution as described in detail elsewhere (17).

TABLE 1

Elemental Composition of the Catalysts

Catalyst	Na (wt%)	$(Si/Al)_{tot}$	Al_F (mmol/g)	Al_{EF} (mmol/g)	Pt (wt%)
Pt/NaY	10	2.5	4.3	0	1.1
Pt/H–USY	0.1	2.5	2.6	2.2	1.05

Note. F = framework; EF = extra-framework.

Conversion of Tetralin

The catalytic experiments were performed in a stirred batch reactor of 250 ml; 100 mg of catalyst was reduced *in situ* at 400°C and added under hydrogen to the feed (100 g, compositions are given below) at RT and 1 bar pressure. The loaded batch reactor was heated to the desired temperature (350°C) and then pressurized to 60 bar hydrogen. Subsequently, the stirring and sampling were started. Samples were taken from the batch for more than 3 h and were analyzed afterward with a gas chromatograph. The catalytic conversion of tetralin was measured in a feed consisting of 3 g of tetralin, 1 g of dodecane as the internal reference, 96 g of hexadecane, and 165 ppm dibenzothiofene. For further details, see (18, 19).

XAFS Spectroscopy

The X-ray absorption spectra at the Pt L_3 and L_2 edge were collected at the Wiggler Station 9.2 of the SRS (Daresbury, UK) using a Si(220) double-crystal monochromator. Experiments were also performed at the ESRF (Grenoble, France) at BM29 using a Si(311) crystal. The monochromator was detuned to 70% of maximum intensity. All measurements were performed in transmission mode using ion chambers filled with Ar to have an X-ray absorbance of 20% in the first and of 80% in the second ion chamber. The samples were pressed into a self-supporting wafer (calculated to have an absorbency of 2.5) and placed in a controlled atmosphere cell operated at 1 atm (20). The samples were reduced in flowing hydrogen at 400°C (heating rate 5°C/min) for 1 h. The samples were evacuated at 200°C for 1 h and XAFS spectra were recorded at liquid nitrogen temperature maintaining a vacuum of better than 2×10^{-5} Pa.

RESULTS

TOF of Tetralin and Neopentane Conversion

The rate of the conversion of tetralin can be expressed with a first-order rate constant ($kg_{feed} kg^{-1}_{catalyst}\ h^{-1}$) with mol of tetralin converted per mol of Pt per second using the initial feed composition. The TOF is defined as the rate (mol of tetralin/(mol of Pt s)) normalized by the H/Pt value determined with hydrogen chemisorption on the freshly prepared catalysts. The lowest values were found for Pt/NaY, whereas the highest values were obtained with the Pt/H–USY. The TOF for Pt/H–USY increases relative to that of Pt/NaY by a factor of 20. The results are plotted in Fig. 1a.

Data for the conversion of neopentane, as published earlier by our group, are given in Fig. 1c for Pt/LTL zeolite (11). The data obtained for amorphous mesoporous supported Pt/SiO_2–Al_2O_3 and Pt/MgO–Al_2O_3 (16) catalysts are shown in Fig. 1e. All plots show that the catalytic properties are a strong function of the composition of the support. For the Pt/Y catalysts the increase can be due to the presence of extra-framework Al, the increase in the Si/Al ratio, and the number of protons. For Pt/LTL the increase is due to the increasing acidity (H^+)/decreasing alkalinity (K/Al ratio) of the LTL zeolite while for the amorphous mesoporous supports the increase is due to a pure decrease in electronegativity. In fact, the increase in TOF for all samples can be correlated with a decrease in the electron charge (decreasing electron richness) of the support oxygen atoms as revealed by the AXAFS.

Background Subtraction, Separation of Double-Electron Excitations (DEE), and Atomic XAFS (AXAFS)

The pre-edge background of the X-ray absorption data was approximated by a modified Victoreen and removed from the raw data. The post-edge background was removed using a very careful background subtraction procedure. The spline technique was applied but with newly developed criteria for separating the double-electron excitations (DEE) and AXAFS contributions. We have shown this previously for Pt/γ-Al_2O_3 (21). A systematic and detailed approach has been developed for Pt foil (22). The method requires the use of a continuous smooth parameter rather than the more usually applied nodal spline technique. The new method of separating the DEE and AXAFS contributions is demonstrated in Fig. 2. The Fourier transform of the raw XAFS data of Pt/H–USY (reduced at 400°C followed by evacuation at 200°C) is displayed in Fig. 2a. The assignments of the peaks below $R < 1.5$ Å are based upon their dependence on the smooth parameter SM (22). The optimum SM value of 0.5 (dotted lines in Fig. 2) leads to a smooth background (see Fig. 2b) and the presence of both DEE and AXAFS peaks in the Fourier transform of the XAFS data. The DEE peaks disappear from the Fourier transform for a SM value of 0.36 (solid line in Fig. 2a) and appear as a small step function around 180–200 eV (solid line in Fig. 2b). A further decrease in SM value results in a decrease of the Pt–Pt peak in Fig. 2a and the appearance of more Pt–Pt EXAFS in the background (dotted dashed lines in Fig. 2). A SM value of 0.36 separates the DEE from the AXAFS. The DEE contributions are present in the background and the AXAFS is contained in the oscillatory part of the spectrum.

EXAFS Analysis and Separation of AXAFS from the Oscillatory Part of the Spectrum

The oscillatory part of the spectrum (AXAFS and EXAFS) is shown in Fig. 3a (solid line). The corresponding Fourier transform (k^2, $2.5 < k < 14$ Å^{-1}) is plotted in Fig. 3b (solid line). The AXAFS contributions overlap with the first-shell Pt–Pt and Pt–O EXAFS contributions. The AXAFS are therefore separated from these EXAFS contributions using the "difference file" technique with fitting in R space (23). Theoretical phase shifts and backscattering

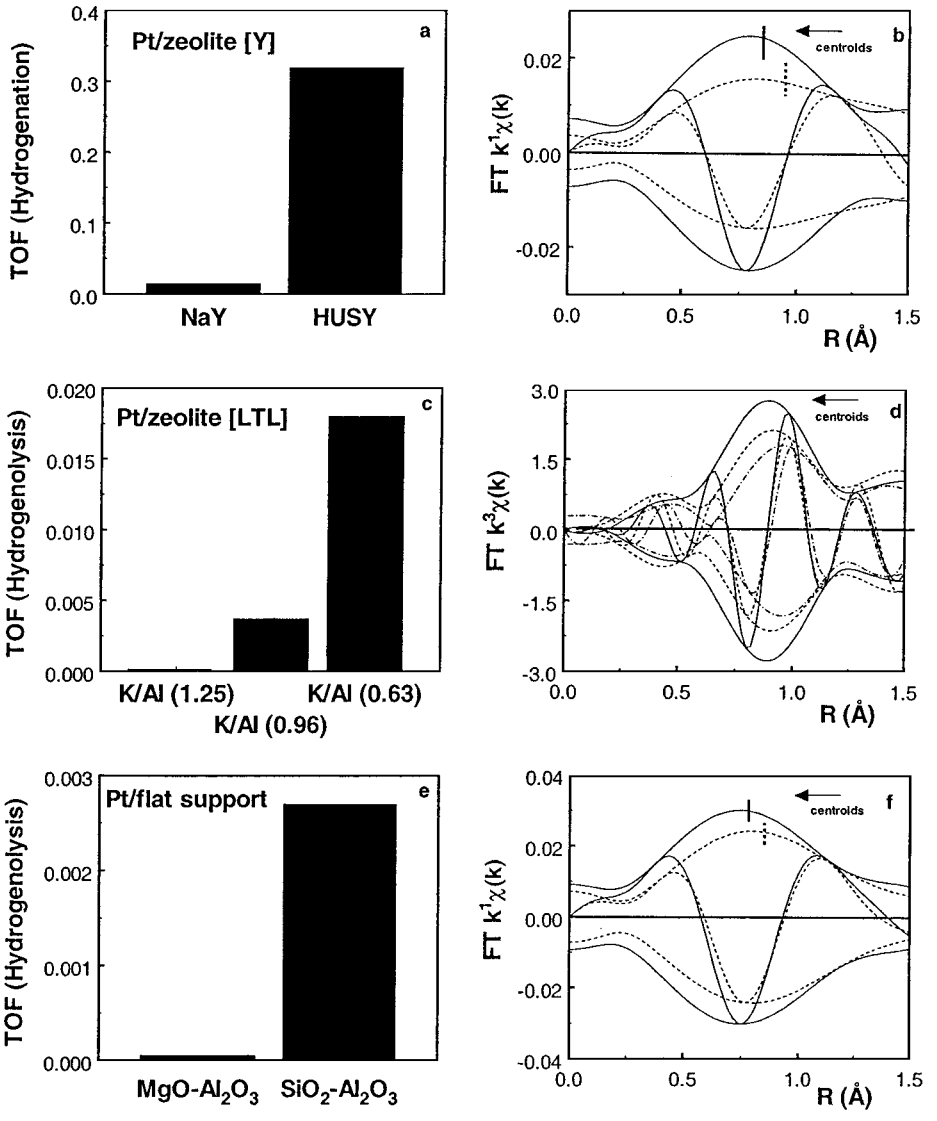

FIG. 1. Correlation between TOF (tetralin and neopentane conversion) and intensity of Fourier transform atomic XAFS peak for different supported Pt catalysts. (a) TOF of tetralin conversion over Pt/H–USY and Pt/NaY catalysts, (b) Fourier transform (k^1, Δk = 2.5–8 Å^{-1}) of atomic XAFS of Pt/H–USY (solid line) and Pt/NaY (dotted line), (c) TOF of neopentane conversion over Pt/LTL catalysts with changing K/Al ratio, (d) Fourier transform (k^3, Δk = 3.0–13 Å^{-1}) of atomic XAFS of Pt/LTL (solid line: K/Al = 0.63, dotted line: K/Al = 0.96, dashed dotted line: K/Al = 1.25), (e) TOF of neopentane conversion over Pt/SiO_2–Al_2O_3 and Pt/MgO–Al_2O_3 catalysts, and (f) Fourier transform (k^1, Δk = 2.5–8 Å^{-1}) of atomic XAFS of Pt/SiO_2–Al_2O_3 (solid line) and Pt/MgO–Al_2O_3 (dotted line) catalysts. Note that the intensity of the FT AXAFS peak increases and the position of the centroid moves to lower R values with decreasing electron charge (decreasing electron richness) of the support oxygen atoms. The increase in intensity and the shift to lower R values of the Fourier transform AXAFS peak is correlated with an increase in TOF.

amplitudes for the Pt–Pt and Pt–O scattering pairs were generated utilizing the FEFF7 (24) code. These phase shifts and backscattering amplitudes were calibrated (25) with the help of XAFS spectra for Pt foil (26) and $Na_2Pt(OH)_6$ (27). Details of the EXAFS analysis of the Pt/Y, Pt/LTL, Pt/SiO_2–Al_2O_3, and Pt/MgO–Al_2O_3 data are given in Refs (8), (11), and (16), respectively. The Pt–Pt coordination parameters after removal of chemisorbed hydrogen are summarized in Table 2.

The presence of AXAFS in the XAFS data is further demonstrated in Fig. 3 for the Pt/H–USY catalysts. The dotted line in the FT represents the fitted Pt–Pt + Pt–O contribution. The differences visible from $0.3 < R < 1.4$ Å are due to the AXAFS contributions in the raw data. The AXAFS contribution can be isolated by subtracting the calculated Pt–Pt and Pt–O contribution from the experimental EXAFS data. The amplitude of the AXAFS function decreases rapidly with increasing k and is within the noise level for $k > 8$ Å^{-1}. The k^1 weighted Fourier transform of the difference file obtained for Pt/H–USY is therefore taken from 2.5 to 8 Å^{-1} (see Fig. 1b, solid line). Inverse Fourier transformation ($0.3 < R < 1.4$ Å) of the Fourier transform shown in Fig. 1b results in the AXAFS oscillations in k space. The AXAFS oscillations are plotted

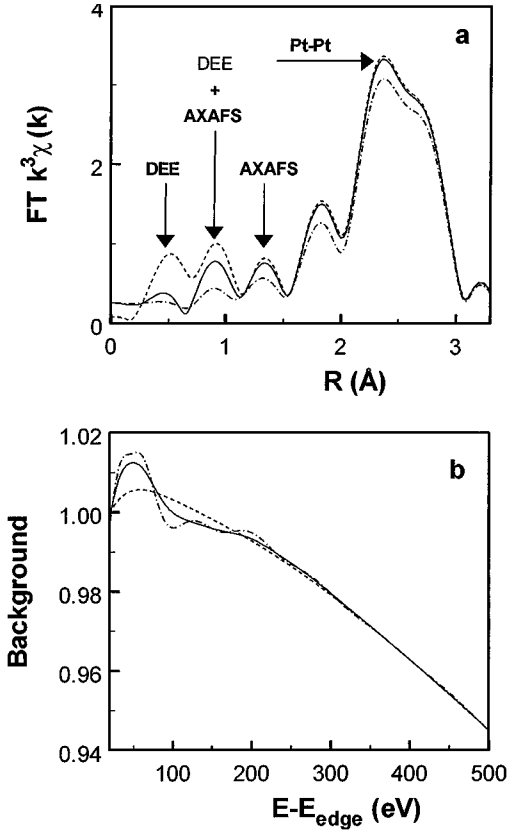

FIG. 2. (a) Fourier transform (k^3, $1.6 < k < 12$ Å^{-1}) of the raw XAFS data of Pt/H–USY (reduction at 400°C followed by evacuation at 200°C) with the smooth parameter (SM) for background removal as an independent parameter: SM = 0.5 (dotted line), SM = 0.36 (solid line), and SM = 0.28 (dashed dotted line). Assignment of peaks for $R < 1.5$ Å based on their dependence on the smooth parameter SM (21). (b) X-ray background absorption for SM = 0.5 (dotted line), SM = 0.36 (solid line), and SM = 0.28 (dashed dotted line) determined during background removal as described in (a). Small step around 180–200 eV represents the double-electron excitation.

in Fig. 3a with a dotted line. It can be seen that at low values of k the amplitude of the AXAFS is about half the Pt EXAFS. This shows also that the new method of background subtraction indeed leads to the appearance of a statistically very significant contribution, which can be further studied.

The amplitude of the AXAFS peak in the Fourier transform of Fig. 1b is larger for Pt/H–USY (solid line) than for Pt/NaY (dotted line). Moreover, the peak centroid shifts to lower R values for the Pt/H–USY sample. Experimental AXAFS data have been published earlier by our group on Pt dispersed in zeolite LTL (11) and Y (8) and on mesoporous amorphous supports (16). The AXAFS data for the Pt/LTL catalysts are shown in Fig. 1d. The data for Pt/SiO_2–Al_2O_3 (solid line) and Pt/MgO–Al_2O_3 (dotted line) are displayed in Fig. 1f. For all supports, the AXAFS peak intensity increases with decreasing electron charge (decreasing electron richness) of the support oxygen atoms.

TABLE 2

EXAFS Fit Results for the Pt–Pt Coordination Determined after Removal of Chemisorbed Hydrogen

Pt–Pt parameters	N	R (Å)
Pt/NaY (evacuation)[a]	5.5	2.64
Pt/H–USY (evacuation)[a]	6.7	2.66
Pt/LTL (0.63) (He TPD)[b]	4.2	2.72
Pt/LTL (0.96) (He TPD)[b]	4.3	2.71
Pt/LTL (1.25) (He TPD)[b]	2.0	2.70
Pt/SiO_2–Al_2O_3 (evacuation)[c]	6.7	2.67
Pt/MgO–Al_2O_3 (evacuation)[c]	7.3	2.71

[a] For further details see (8).
[b] For further details see (11).
[c] For further details see (16).

Calculated AXAFS Data

To interpret these effects, we have performed quantum mechanical *ab initio* multiple scattering cluster calculations with the FEFF7 code using a tetrahedral Pt_4 cluster supported on a surface, mimicked here by three O atoms in a plane as a model catalyst (see Fig. 4). Here, the Pt–O distance was set at 2.25 Å. The charge on the "support"

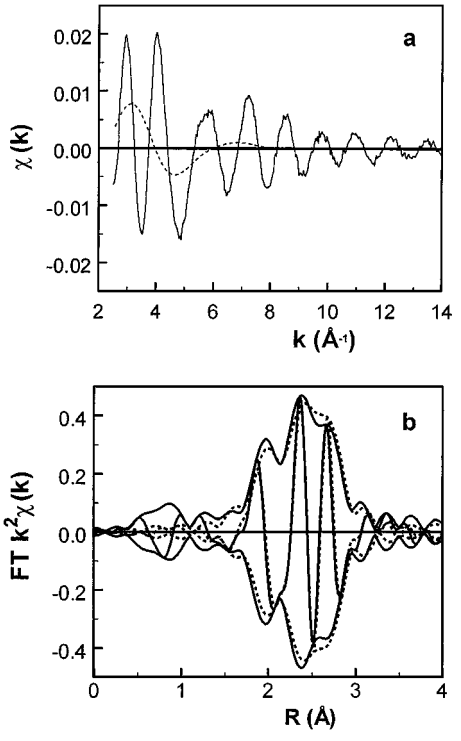

FIG. 3. (a) XAFS data (EXAFS plus AXAFS) of Pt/H–USY (reduction at 400°C followed by evacuation at 200°C) (solid line) and isolated AXAFS (see text) (dotted line). (b) Fourier transform (k^2, $2.5 < k < 14$ Å^{-1}) of the EXAFS data of Pt/H–USY (reduction at 400°C followed by evacuation at 200°C) (solid line) and of the model EXAFS (Pt–Pt + Pt–O) obtained by R space fit to the experimental data in the region $1.6 < R < 3.1$ (dotted line). The remaining AXAFS peak is visible around $R = 0.75$ Å.

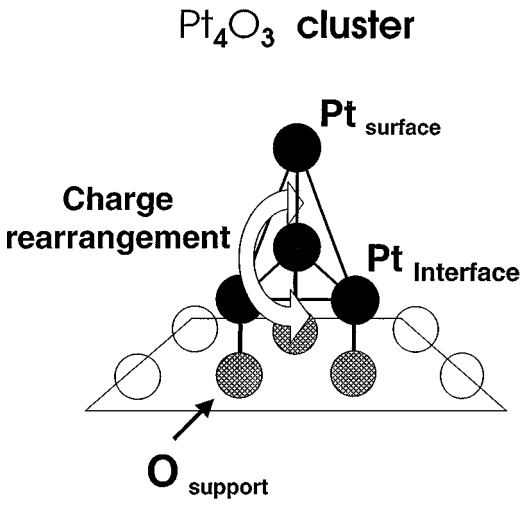

FIG. 4. Schematic illustration of Pt_4O_3 cluster for which the FEFF7 calculations were performed. The arrow represents the charge rearrangement induced by the support oxygen atoms as discussed in the text.

oxygen atoms was assumed to be +0.05, 0.00, and −0.01 electron. The FEFF7 code calculates a full X-ray absorption spectrum for each type of Pt atom in the cluster, viz. Pt interface (Pt_{int}) and Pt surface (Pt_{surf}). These calculations do not allow for simple charge transfer between the Pt and O atoms, but certainly includes the polarization of the Pt atoms by the O atom charge. Isolating the AXAFS from the full spectrum in a procedure identical to that used for the experimental data, as described above, and averaging Pt_{surf} and $3Pt_{int}$ produces the theoretical average AXAFS. The Fourier transform of this theoretical XAFS spectrum is given in Fig. 5. The theoretical data can be compared with the experimental data as shown in Fig. 1. Note that not only the increase in the AXAFS but also the shift in the centroid to lower

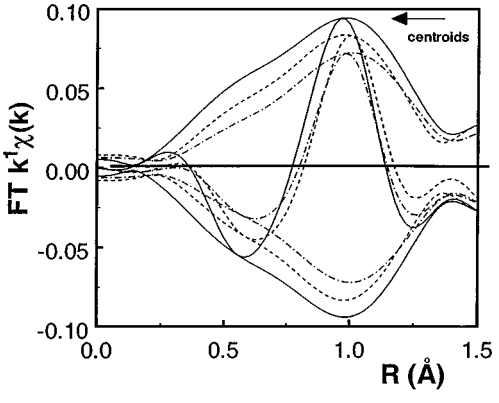

FIG. 5. Fourier transform (k^1, $\Delta k = 2.5$–10 Å^{-1}) of AXAFS as determined by *ab initio* multiple scattered wave calculations using the FEFF7 code when the charge on the O support atoms was assumed to be +0.05 (solid line), 0.00 (dotted line), and −0.01 (dashed dotted line) of an electron as indicated.

R with increasing positive oxygen charge, is qualitatively reproduced.

We note that the average Pt–Pt and Pt–O coordination numbers for this Pt_4O_3 cluster are 3 and 0.75, respectively. The Pt–O coordination number here is somewhat bigger than that seen in the experimental data, but even with a single O atom, giving a Pt–O number of 0.25, and closer to that seen experimentally, the magnitude of the changes in the AXAFS can still be reproduced, albeit with slightly bigger charges on the single O atom.

DISCUSSION

TOF of Tetralin and Neopentane Conversion

Figures 1a, 1c, and 1e show that the TOF of the catalysts strongly depend on the composition of the support. Neopentane hydrogenolysis is a monofunctional probe reaction, dependent only on the catalytic activity of the metal (28, 29) as confirmed by the primary reaction products: methane, isobutane (hydrogenolysis), and isopentane (isomerisation). Neopentane does not undergo protolytic cracking at the temperatures used for the catalytic reaction (250°C). Neopentane hydrogenolysis cannot occur via a bifunctional mechanism because the neopentane molecule cannot form an alkene intermediate. Therefore, the changes in the TOF cannot be ascribed to a bifunctional mechanism. A bifunctional mechanism has been proposed for the conversion of aromatics over Brønsted acid sites (30) in order to explain the higher activity of acidic supported Pt catalysts. However, as shown elsewhere (18), the increase in TOF for tetralin conversion cannot be correlated with the number of Brønsted acid sites alone. A much larger increase is observed as a result of increasing the polarization power of the charge-compensating cations. Detailed studies (18, 19) also show that the increase in TOF of both reactions cannot be related to a change in absorption and diffusion properties of the support or to an influence of Pt particle size effects. All these results strongly indicate that only the Pt catalyzes the conversion of tetralin and neopentane.

The activities for the hydrogenation of tetralin as a function of the support properties follow the same trend as previously observed with the activities for neopentane conversion in hydrogen over Pt/LTL (11) and Pt/Y (8) catalysts. Moreover, the activities for the conversion of neopentane in hydrogen after sulfur poisoning of Pt/LTL (31) and Pt/Y, with and without H_2S in the feed (19), show the same dependence with the composition of the support. Therefore, it is very likely that the influence of the composition of the support, and in particular the electron richness of the support oxygen atoms, directly influences the catalytic properties of the Pt particles. The expected influence of the support, and its electron richness, on the electronic properties of the supported Pt particles is discussed in the following section.

Insight from Experimental AXAFS and FEFF7 Results

Ramaker *et al*. (12) and others (32–34) have previously discussed the origin and the parameters determining the AXAFS. The AXAFS is caused by scattering of the photoelectron off the deep valence electrons in the absorbing atom periphery. From a more physical point of view, the photoelectron scatters against the embedded atom potential barrier, $U_{\mathrm{emb}}(R)$, which effectively exists between the photoelectron and the nuclei screened by its surrounding electrons. The embedded atom potential is the sum of its own (the absorbing atom) potential and those surrounding the absorber atom as a result of being embedded in the system. The well-known muffin-tin approximation can be used to approximate the embedded atom potential (see Fig. 6a). This approximation "clips" the exact potential at the muffin-tin radius R_{mt} and sets it equal to the interstitial potential V_{int} (12). Inside R_{mt} the potential is assumed to be spherical; outside, it is assumed to be flat and zero (i.e., no forces are exerted on the particle in the interstitial region). V_{int} is determined by averaging the potential at R_{mt} of all the atoms in the cluster, and this determines the zero of energy or the effective bottom of the conduction band. The role of V_{int} is illustrated in Fig. 6a.

The AXAFS directly reflects the position and shape of this interatomic potential. Basically, a phase-corrected and k-weighted Fourier transform of the measured or calculated AXAFS function $\chi_{\mathrm{AX}}(k)$ leads to (12)

$$\left|(2\pi)^{-1/2}\int e^{-ikR}\left[ke^{-2i\delta(k)}\chi_{\mathrm{AX}}(k)\right]dk\right| \approx \Delta U(R) * \Gamma(R), \qquad [1]$$

where $\Delta U(R) = U_{\mathrm{emb}}(R) - U_{\mathrm{free}}(R)$ with $U_{\mathrm{emb}}(R)$ and $U_{\mathrm{free}}(R)$ the embedded and free atom potentials as shown in Fig. 5a and $\Gamma(R)$ a broadening function due to the limited Fourier transform range. Here, the $*$ indicates the convolution of the two functions, $\Delta U(r) * \Gamma(R) = \int \Delta U(r)\,\Gamma(R\text{-}r)\,dr$. The free atom potential reflects the electron distribution in the free atom (which of course does not change with the support), whereas the embedded potential reflects the electron distribution after embedding the free atom into its chemical environment and allowing interaction with its neighbours. Equation [1] then reveals that the FT directly reflects this change in the chemical environment. More specifically, the shape and intensity of the |FT| can be represented by the area between $U_{\mathrm{free}}(R)$ and $U_{\mathrm{emb}}(R)$ and below $V_{\mathrm{cut}}(V_{\mathrm{cut}} = 2 * V_{\mathrm{int}} + |E_f|)$ as illustrated in Fig. 6a (for further detailed information see (8, 12)). In the FT results to be presented below, phase correction is not actually carried out (i.e., the $e^{-2i\delta(k)}$ factor is ignored) since it alters only the imaginary part of the FT, and we are quantitatively just interested in the absolute value.

Since the Fourier transform of $\chi_{\mathrm{AX}}(k)$ is directly proportional to $\Delta U(R) = U_{\mathrm{emb}}(R) - U_{\mathrm{free}}(R)$, the shape and intensity of the AXAFS peak directly reveals electronic and chemical bonding information, such as the electronic charge (e.g., that resulting from simple charge transfer off the cluster), the extent of bonding of supported metal particles with support oxygen atoms, and direct Coulomb field effects such as that resulting from the metal–support interaction. Thus, changes in the Pt AXAFS with support should directly reflect the potential interaction between the Pt particle and the support. The quantum mechanical *ab initio* scattered-wave (SW) cluster code, FEFF7, as utilized in this work, has the full mathematical evaluation of the AXAFS contributions within the muffin-tin (MT) approximation (12). Comparison with *ab inito* molecular orbital calculations from the literature, which we present below, enables determination of the essence of the metal–support interaction from a chemical bonding point of view.

The effect of the electron charge (the electron richness) of the support oxygen atoms on the AXAFS can be understood by using Figs. 6a and 6b. This figure shows the changes in the interatomic potential curves with an increase and decrease of the electron charge (charge on the O atoms in our FEFF7 cluster calculation) that directly lead the changes in

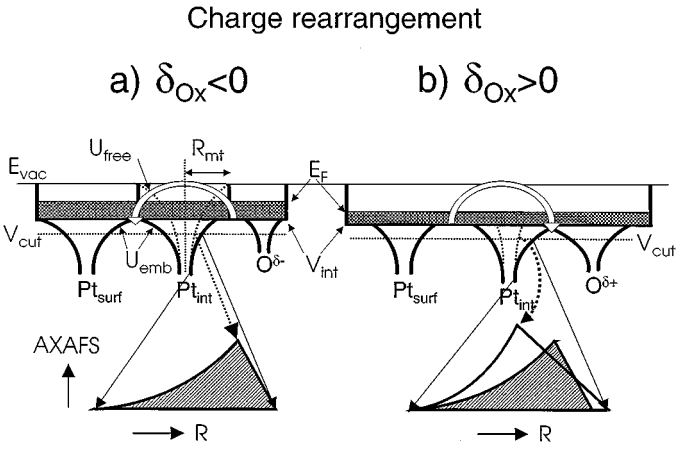

FIG. 6. (a) Illustration of the muffin-tin approximation to the interatomic potentials showing the muffin-tin radius R_{mt} and locations of V_{int}, E_{F}, E_{vac}, and V_{cut}. Solid potential curves indicate embedded atom potential (U_{emb}); dotted potential curve for absorber Pt atom indicates free atom potential (U_{free}). The potentials for an interfacial Pt atom are influenced by the potential of a support oxygen ion. The intensity of the Fourier transform AXAFS peak is represented by the area between U_{emb} and the free atom potential (U_{free}) and below V_{cut}, as illustrated by the enlarged shaded area. The presence of an "electron-rich" ($\delta_{\mathrm{Ox}} < 0$) support oxygen atom causes a charge rearrangement from the oxygen atoms in the metal–support interface to the Pt metal particles, as indicated by the curved arrow. (b) A schematic illustration of the charge rearrangement effect due to an "electron-poor" ($\delta_{\mathrm{Ox}} > 0$) support oxygen atom and its influence on the shape and intensity of the Fourier transform AXAFS peak. The curved arrow represents the charge rearrangement from the metal particle to the oxygen atoms in the metal–support interface. Note the steeper and broader potential well for oxygen and interfacial Pt for the electron-poor oxygen case. Note also the smaller Pt–Pt potential overlap (smaller electron density) and larger Pt–O overlap (larger electron density) below V_{cut} when the electron charge of the support oxygen atoms decreases.

the Fourier transform of the AXAFS. Note first of all the steeper potential gradient on the right compared to that on the left. These effects are greatly exaggerated in the figure to provide more clarity. The nearby interfacial Pt atoms (Pt_{int}) experience this larger potential gradient, which causes an increased curvature to higher binding energy of the Pt_{int} potential. This increases the AXAFS amplitude and changes it shape. In addition, the incremental positive charge on the support oxygen increases its electronegativity, which attracts additional electronic charge from within the Pt cluster to the cluster–support interface. This charge rearrangement is represented in the muffin-tin approximation by the lowering of V_{int} and therefore V_{cut}. This causes the shift, ΔR, in the centroid to lower values of R. Note that the peak in $\Delta U(R)$ appears near the MT radius (which for Pt occurs around 1.53 Å and for O at 0.98 Å when assuming a Pt–O distance of 2.2 Å), and the convolution of $\Delta U(R)$ with $\Gamma(R)$ causes the peak to become rounded and appear at lower R. Since the ultimate peak position is therefore dependent on $\Gamma(R)$, we prefer to note the centroid of the AXAFS, which is much less dependent on $\Gamma(R)$.

Insights from MO Results

High level *ab initio* molecular orbital (MO) calculations on Pt clusters (35, 36) and the adsorption of small adsorbates [H (37, 38), H_2 (39), O (40), OH (40, 41), CO (42, 43), H_2O (41), CH_4 (44), CH_x and C_2H_x (38), and NH_3 (41)] on the "surface" of these clusters have recently been published. These calculations use different levels of approximation (e.g., density functional theory, DFT (40, 41, 43), or generalized valence bond, GVB (35, 38), theory). However, they all use some approximate linear combination of atomic orbitals to construct the molecular orbitals (LCAO-MO). In contrast, the FEFF code uses the scattered-wave muffin-tin (SW-MT) approximation. The SW-MT results are more easily discussed in the context of the AXAFS data because they provide spherically averaged potential curves such as those indicated schematically in Fig. 5. However, these previously published MO results can provide further insight in terms of changes in electronic structure of the metal particles induced by changes in the support (45).

The MO results for an isolated metal cluster indicate that the Pt 6*sp* orbitals overlap strongly forming bonding and antibonding MOs or bands which are positioned on both sides of the 5*d* band (35, 38, 40, 41). Consistent with this, Kua and Goddard (35, 38) suggest that the 6*s* orbitals form "interstitial bond orbitals" (IBO and IBO*), in contrast to the 5*d* orbitals that are almost nonbonding, giving a narrower overall *d* band. In bulk metal or in clusters, one IBO forms at the center of half of the Pt_4 tetrahedra in the solid (35). In a tetrahedral Pt_4 cluster, the four Pt 6*s* orbitals would form symmetry-adapted linear combinations (SALCs) of A_1 and T_2 symmetry. The lowest occupied IBO has A_1 symmetry

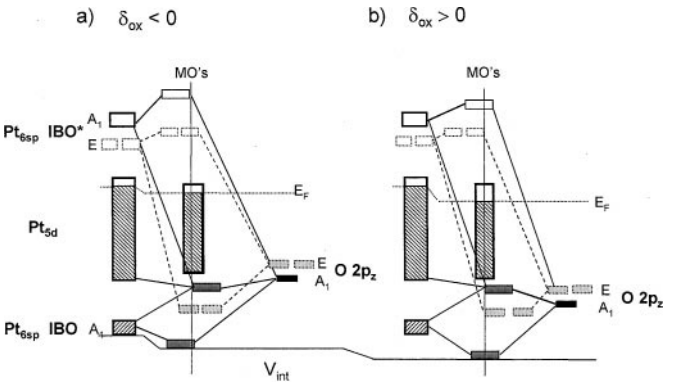

FIG. 7. (a) Schematic molecular orbital density of states as determined from the symmetry restrictions on a Pt_4O_3 cluster as shown in Fig. 4 and the various MO calculations referenced in the text. Note the existance of the interstitial bond orbitals IBO (A_1) and IBO* (E and A_1) formed from the Pt *6s* orbitals and the relatively narrow 5*d* band. The bonding IBO–O2p_z (E and A_1) MO appears at the bottom of the conduction band (therefore it locates V_{int} used in the SW-MT approximation). The horizontal location of the MOs relative to the vertical line between the Pt and O qualitatively indicate the relative component of each atomic orbital in the MO. For the "electron-rich" ($\delta_{Ox} < 0$) support oxygen case the lowest E MOs are mixed Pt 6*s* IBO* and O $2p_z$ SALCs. This mixing represents a net charge movement from the oxygen in the metal–support interface to the IBOs of the Pt particles. (b) In the "electron-poor" ($\delta_{Ox} > 0$) support oxygen case the mixing of the A_1 Pt 6*s* IBO with the A_1 O $2p_z$ results in a charge rearrangement from the Pt particles to the oxygens in the metal–support interface.

and three degenerate empty IBO*s have T_2 symmetry. The spatial position of the occupied A_1 IBO orbital is in the middle of the Pt_4 cluster shown in Fig. 4.

The Pt_4O_3 cluster utilized in this work has C_{3v} point group symmetry so that the four Pt 6*s* orbitals now form SALCs of A_1, E, and A_1 symmetry, as shown in Fig. 7. The three O $2p_z$ orbitals are taken parallel to the C_{3v} axis and they determine the interaction with the Pt cluster. The O $2p_x$ and O $2p_y$ orbitals, pointing perpendicular to this axis (parallel to the support), are involved in the bonding within the support and hence can be ignored here. The three O $2p_z$ orbitals form SALCs of A_1 and E symmetry, as shown in Fig. 7. The three A_1 and two E SALCs can then mix separately, forming the MOs as schematically shown. The SALCs and MOs of E symmetry are shown with dotted lines and those of A_1 symmetry as solid lines in Fig. 7.

The orbital mixing proposed and illustrated here is based on the results of Chen *et al.* (40) for O and OH adsorbates on an isolated Pt_{10} cluster, along with the restrictions required by symmetry arguments in the highly symmetric Pt_4O_3 cluster. Their results indicate that both the bonding and antibonding (Pt 5*d*)–(O $2p$) MOs are nearly filled so that little net bonding occurs between O $2p_z$ and the Pt 5*d* orbitals. They suggest that the net OPDOS (overlap population DOS) is indeed slightly negative. Thus, we ignore the Pt 5*d* orbital bonding in Fig. 7a, except as noted below.

Extrapolating previous MO results to the current work suggests that the seven MOs resulting from the SALCs described above remain nearly unmixed with the Pt 5*d* orbitals, except for the A_1 MO falling very near the bottom of the 5*d* band and perhaps a little with the *E* MOs. In Fig. 7 the estimated amount of mixing of each SALC in the MO is qualitatively estimated by the relative energy difference between the SALCs and the resultant MO. The extent of this mixing is indicated by the horizontal position of the MO relative to the vertical line.

In the electron-rich case (incremental charge less than zero) the lowest A_1 MO is mostly localized on the Pt 6*s* IBO, while the lowest *E* MOs are mixed Pt 6*s* IBO* and O $2p_z$ SALCs. Note that initially the Pt 6*s* IBO* *E* SALCs were empty and the O $2p_z$ *E* SALCs were full. This mixing represents a net charge movement from the oxygen to the metal–support interface. In the electron-poor case the lowest *E* MOs revert back to primarily O $2p_z$ *E* SALCs. The lowest A_1 MO now consists of Pt 6*s* IBO and O $2p_z$ A_1 SALCs representing a net charge movement from the Pt cluster to the metal–support interface. These charge rearrangements are schematically represented in Fig. 4 with the curved arrow. Note that the mixing indicates a stronger bonding interaction between the cluster and the support in the electron-poor case. The Pt 5*d* orbitals experience the transfer of charge away from or to the Pt metal to the metal–support interface. Thus, the ionization potential of the *d* band increases and the *d* band narrows some, as shown in both Figs. 6 and 7 as the support becomes more incrementally charged (less electron rich).

These MO results are consistent with the AXAFS and SW-MT results from FEFF7, which also suggest a movement of charge from the Pt interstitial region to the cluster–support interface region with increased incremental charge. The MO results indicate that this charge is primarily Pt 6*s* in character. In the FEFF7 results, the downward shift in V_{int} signifies this charge transfer and reflects a shift in the bottom of the conduction band, i.e., exactly the location of the Pt 6*s* or IBO orbitals, as illustrated in Fig. 7b.

GVB calculations (35) indicate that the IBOs dictate the electron density in the 5*d* orbitals since the formation and filling of the IBOs determine the 5*d* orbital filling. Therefore, in the MO picture, the charge rearrangement alters the 5*d* electron density, as illustrated in Fig. 7. It will be shown in a forthcoming paper that the metallic character of the cluster is indeed determined by this charge rearrangement (46) and the nature of the support. Thus, both the Fermi level and the entire valence band (Pt 5*d* and Pt 6*sp*) shift to higher binding energy, as illustrated in Fig. 7.

Fahmi and van Santen (41) have reported MO calculations for Pt_6OH and Pt_6OH_2 clusters. The Pt–O distance for the Pt_6–OH_2 case was calculated (41) to be around 2.3–2.4 Å, comparable to the Pt–O distance (2.25 Å) found in our previous EXAFS results (47, 48). This would suggest that the magnitude of the covalent interaction is comparable to that for the metal–support interaction. Of course, the O atoms in the support are bonded to two Si atoms (or a Si and a Al), but the two H atoms in the Pt_6OH_2 cluster reasonably model these Si atoms. Thus, these MO results might serve as a reasonable model for the Pt–support O interaction. Their calculations show that H donates electron density to the O atom; therefore, the O in the Pt_6OH cluster has the more positive charge. In this comparison Pt_6–OH roughly approximates the electron poor or $\delta > 0$ and Pt_6–OH_2 the electron rich or $\delta < 0$.

Their calculated results show the same trend in charge rearrangement with support acidity, as suggested by Fig. 7. The total charge transfer is 0.36 electron toward the OH ("acidic $\delta > 0$") vs 0.09 electron away from the H_2O ("basic $\delta < 0$"), exactly the directions expected for acidic and basic supports relative to neutral supports. Further, the magnitude of these charges is comparable to those we used to model the AXAFS changes in Fig. 5. However, the MO picture suggests that the charge rearrangement occurs in the very diffuse A_1 and *E* MOs, not in the local Pt 5*d* orbitals. Elsewhere (8), we showed that a complete charge transfer from the 5*d* band of the cluster to the support would not produce the ΔR shift seen in both the experimental AXAFS and the FEFF7 theoretical AXAFS. On the other hand, both a 5*d* band charge transfer and the direct Coulomb field, in the case of no charge transfer as assumed in FEFF7, will increase the AXAFS because both produce a shift in the Pt valence orbitals. Thus, the extent of charge transfer cannot be ascertained directly from the magnitude of the AXAFS. On the other hand, the AXAFS ΔR shift is consistent with the "incomplete" delocalized charge rearrangement model suggested by the MO analysis.

Recent GVB-MO calculations (38) indicate that the Pt–H bond has a strong component of both the Pt 5*d* and the Pt 6*sp* orbitals. In contrast, the bonding of Pt with various alkane radicals (i.e., alkanes with one H removed) appears to be generally determined by localised bonding between the carbons and the Pt 5*d* orbitals (38). A shift in the Pt 5*d* orbitals will certainly alter the strength of the Pt–C bond as well. Thus, the change in the TOF for neopentane and tetralin conversion, as reported above, could result from either the shift in Pt 5*d* orbital binding energy, the charge rearrangement effect involving the IBOs, or a combination of both effects. The exact role of each has yet to be elucidated.

The interpretation of the AXAFS results as presented in this paper and confirmed by previously reported MO calculations in the literature are being further elucidated by *ab intio* self-consistent field real space multiple scattering calculations (FEFF8(49)) to be reported elsewhere (46). Preliminary results for the density of states show similar trends, as illustrated in Fig 7.

Implications for Catalysis and Preparation of Tailor-Made Catalysts

The correlation between the electron charge of the support oxygen atoms and the catalytic properties (e.g., TOF) of supported Pt particles has been established in this work and in earlier studies of our group. It was also found that the electron charge of the support oxygen atoms influences the electronic structure of the supported Pt particles as seen in the AXAFS. On the other hand, an understanding of the relationship between the change in electronic structure of the Pt surface where the catalysis occurs and the change in the Pt catalytic properties still has to be elucidated. However, several strong arguments for a direct relationship can be inferred from this and other results published previously by our group.

(1) It has been shown that the surface–adsorbate bond strength correlates with the electron richness of the support oxygen atoms. For example, the results of the analysis of the Pt–H shape resonances (8, 14) show that the Pt–H bonding is changing with decreasing electron charge of the support oxygen atoms.

(2) Further, the type of bonding correlates with the electron charge as shown by FTIR of chemisorbed CO on Pt/LTL and Pd/LTL. With decreasing electron charge of the support oxygen atoms the ratio of linear/bridged bonded CO on Pt and Pd increases (9, 10), demonstrating that the type of Pt–CO bonding is changing.

(3) The results of neopentane kinetic studies (19) can be understood by an increasing number of adsorbed neopentane intermediates that undergo only a single dehydrogenation step (i.e., increasing ratio of single- to double-bonded intermediate species) with decreasing electron charge of the support oxygen atoms.

(4) The TOF for the hydrogenation of the aromatic ring of tetralin increases when a higher amount of adsorbed intermediates exists on the surface of Pt. With decreasing electron charge of the support oxygen atoms the ionization potential of the Pt valence orbitals is increasing, thereby increasing their electron-acceptor capacity. The number of tetralin intermediates increases when increased π electron donation into the empty d orbitals of Pt is possible.

An understanding of the relationship between the bonding of the catalytic intermediates on the Pt particle surface and the composition of the support must be further elucidated in other studies, but the evidence above strongly indicates that such a relationship exists.

The results of this study imply that by changing the composition of the support of supported metal catalysts, tailor-made catalysts can be prepared. For a catalytic reaction with catalytic intermediates that need metal surface valence orbitals with electron acceptor or donor properties, a metal-supported catalyst has to be prepared on a support with oxygen atoms having a smaller or higher electron charge. The electron negativity of the support oxygen atoms is important. For zeolitic supports the composition can be tuned by introducing protons, changing cations, and Si/Al ratio or by steaming, which leads to the presence of extra-framework Al. For instance, a catalyst for aromatic saturation can be made sulfur tolerant (high catalytic activity in the presence of sulfur) by making the support acidic, by increasing the polarization power of the charge-compensating cations, by decreasing the Si/Al ratio, and by introducing extra-framework Al.

CONCLUSIONS

Recent AXAFS studies along with catalytic data for neopentane conversion have established that the critical aspect of the metal–support interaction for hydrogenolysis/isomerization is a shift in the ionization potential of the metal valence orbital electrons with the electron charge of the support oxygen atoms. The influence of the composition of the support on the catalytic properties of supported Pt particles has been further investigated in a recent study for the hydrogenation of tetralin (HDA) under conditions comparable to process conditions for deep hydrotreatment of diesel. We showed that the support composition still determines the catalytic properties of the metal particles, even in the presence of chemisorbed sulfur. In this study we show that the critical aspect of the metal–support interaction for deep hydro-de-aromatization is also a shift in the ionization potential of the metal valence orbital electrons due to a change of the electron charge of the support oxygen atoms.

Calculations of the AXAFS spectra with the FEFF7 code are found to be in qualitative agreement with the experimental data, reproducing not only the change in intensity but also the change in shape as characterized by a ΔR shift in the centroid of the AXAFS intensity. The Coulomb field of the support as well as a charge rearrangement from the metal particle to the oxygens of metal–support interface or vice versa shifts the Pt valence orbitals. This Pt orbital shift is directly reflected in the intensity of the AXAFS. The rearrangement of charge from the Pt cluster to the metal–support interface and vice versa causes the ΔR shift in the centroid of the FT AXAFS peak. The results of FEFF7 AXAFS calculations and group theory arguments on a highly symmetric Pt_4O_3 cluster, along with previously published molecular orbital calculations, make it possible to derive an MO scheme for the metal–support interaction. The rearrangement of charge from the particle to or from the metal–support interface occurs primarily via the delocalized Pt 6*s* orbitals. The relationship of these changes in Pt electronic structure to the catalytic behavior and the consequences of the metal–support interaction for preparing tailor-made catalysts are discussed.

REFERENCES

1. Karpinski, Z., Gandhi, S. N., and Sachtler, W. M. H., *J. Catal.* **141**, 337 (1993).
2. Zhang, Z., Wong, T. T., and Sachtler, W. M. H., *J. Catal.* **128**, 13 (1991).
3. Larsen, G., and Haller, G. L., *Catal. Lett.* **3**, 103 (1989).
4. de Mallmann, A., and Barthomeuf, D., *J. Chem. Phys.* **87**, 535 (1990).
5. de Mallmann, A., and Barthomeuf, D., *Stud. Surf. Sci. Catal.* **46**, 429 (1989).
6. Jansen, A. P., and van Santen, R. A., *J. Phys. Chem.* **94**, 6764 (1990).
7. Sanchez-Marcos, E., Jansen, A. P. J., and van Santen, R. A., *Chem. Phys. Lett.* **16**, 399 (1990).
8. Koningsberger, D. C., de Graaf, J., Mojet, B. L., Ramaker, D. E., and Miller, J. T., *Appl. Catal. A* **191**, 205 (2000).
9. Mojet, B. L., Kappers, M. J., Meyers, J. C., Niemantsverdriet, J. W., Miller, J. T., Modica, F. S., and Koningsberger, D. C., *Stud. Surf. Sci. Catal.* **84**, 909 (1994).
10. Mojet, B. L., Kappers, M. J., Miller J. T., and Koningsberger D. C., *in* "Proceedings, 11th International Congress on Catalysis, Baltimore, 1996" (J. W. Hightower, W. N. Delgass, E. Iglesia, and A. T. Bell, Eds.), Studies in Surface Science and Catalysis, Vol. 101, p. 1165. Elsevier, Amsterdam, 1996.
11. Mojet, B. L., Miller, J. T., Ramaker, D. E., and Koningsberger, D. C., *J. Catal.* **186**, 373 (1999).
12. Ramaker, D. E., Mojet, B. L., Koningsberger, D. C., and O'Grady, W. E., *J. Phys.: Condens. Matter.* **10**, 8753 (1998).
13. Ramaker, D. E., Mojet, B. L., Garringa Oostenbrink, M. T., Miller, J. T., and Koningsberger, D. C., *Phys. Chem. Chem. Phys.* **1**, 2293 (1999).
14. Mojet, B. L., Ramaker, D. E., Miller, J. T., and Koningsberger, D. C., *Catal. Lett.* **62**, 15 (1999).
15. Koningsberger, D. C., Oudenhuijzen, M. K., Bitter, J. H., and Ramaker, D. E., *Top. Catal.* **10**, 167 (2000).
16. Koningsberger, D. C., Oudenhuijzen, M. K., Ramaker, D. E., and Miller, J. T., *in* "Procedings, 12th International Congress on Catalysis, Granada, 2000" (A. Corma, F. V. Melo, S. Mendioron, J. L. G. Fierro, Eds.), Studies in Surface Science and Catalysis, Vol. 130, p. 317. Elsevier, Amsterdam, 2000.
17. de Graaf, J., van Dillen, A. J., de Jong, K. P., and Koningsberger, D. C., *J. Catal.*, in press.
18. de Graaf., J., Waller, P., van Veen, J. A. R., Ramaker, D. E., and Koningsberger, D. C., in preparation.
19. de Graaf, J., Ph.D. thesis, Utrecht University, 2001.
20. Vaarkamp, M., Mojet, B. L., Modica, F. S., Miller, J. T., and Koningsberger, D. C., *J. Phys. Chem.* **99**, 16067 (1995).
21. Ramaker, D. E., van Dorssen, G. E., Mojet, B. L., and Koningsberger, D. C., *Top. Catal.* **10**, 157 (2000).
22. van Dorssen, G. E., Ramaker, D. E., and Koningsberger, D. C., submitted for publication.
23. Koningsberger, D. C., Mojet, B. L., van Dorssen, G. E., and Ramaker, D. E., *Top. Catal.* **10**, 143 (2000).
24. Zabinsky, S. I., Rehr, J. J., Ankudinov, A., Albers, R. C., and Eller, M. J., *Phys. Rev. B* **52**, 2995 (1995).
25. van Dorssen, G. E., Ph.D. thesis, Utrecht University, 1999.
26. Wyckoff, R. W. G., "Crystal Structures," 2nd ed., Vol. I. Wiley, New York, 1963.
27. Trömel, M., and Lupprich, E., *Z. Anorg. Chem.* **160**, 414 (1975).
28. Davis, S. M., and Somorjai, G. A., *in* "The Chemical Physiscs of Solid Surfaces and Heterogeneous Catalysts" (D. A. King, and D. P. Woodruff, Eds.), Vol. 4, p. 271. Elsevier, Amsterdam, 1982.
29. Anderson, J. R., and Avery, N. R., *J. Catal.* **16**, 315 (1967).
30. Lin, S. D., and Vannice, M. A., *J. Catal.* **143**(2), (1) 539, (2) 554, (3) 562 (1993).
31. Koningsberger, D. C., and Miller, J. T., *J. Catal.* **162**, 209 (1996).
32. Holland, B. W., Pendry, J. B., Pettifer, R. F., and Bordas, J., *J. Phys. C* **11**, 633 (1978).
33. Rehr, J. J., Booth, C. H., Bridges, F., and Zabinsky, S. I., *Phys. Rev. B* **49**, 12347 (1994).
34. Rehr, J. J., Zabinsky, S. I., Ankudinov, A., and Albers, R. C., *Physica B* **208–209**, 23 (1995).
35. Kua, J., and Goddard, W. A., III, *J. Phys. Chem. B* **102**, 9481 (1998).
36. Xu, W., Schierbaum, K. D., and Goepel, W., *Int. J. Quantum Chem.* **62**, 427 (1997).
37. Hammer, B., and Nørskov, J. K., *Nature* **376**, 238 (1995).
38. Kua, J., and Goddard, W. A., III, *J. Phys. Chem. B* **102**, 9492 (1998).
39. Hammer, B., and Nørskov, J. K., *Surf. Sci.* **343**, 211 (1995).
40. Chen, M., Bates, S. P., van Santen, R. A. and Friend, C. M., *J. Phys. Chem. B* **101**, 10052 (1997).
41. Fahmi, A., and van Santen, R. A. *Z. Phys. Chem.* **197**, 203 (1996).
42. Illas, F., Zurita, S., Marquez, A. M., and Rubio, J., *Surf. Sci.* **376**, 279 (1997).
43. Watwe, R. M., Spiewak, B. E., Cortright, R. D., and Dumesic, J. A., *Catal. Lett.* **51**, 139 (1998).
44. Akinaga, Y., Taketsugu, T., and Hirao, K. J., *Chem. Phys.* **107**, 415 (1997).
45. The MO results do not necessarily agree quantitatively with each other and unfortunately are much more computationally laborious. However, they do provide valuable chemical insight and now with the high level of calculation generally agree semiquantitatively with experimental trends. The SCF-Xα calculations, a subset of SW-MT calculations, on Pt_{13} clusters were shown over 20 years ago to provide remarkable agreement with experimental photo-emission data [Messmer, R. P., Knudson, S. K., Johnson, K. H., Diamond, J. B., and Yang, C. Y., *Phys. Rev. B* **13**, 1396 (1976)]. For other applications, however, the results of MT and Xα approximations have to be treated with some skepticism.
46. Ramaker, D. E., Oudenhuijzen, M. K., and Koningsberger, D. C., to be published.
47. Vaarkamp, M., Modica, F. S., Miller, J. T., and Koningsberger, D. C., *J. Catal.* **144**, 611 (1993).
48. *in* "X-ray Absorption Fine Structure for Catalysts and Surfaces" (D. C. Koningsberger, M. Vaarkamp, A. Muñoz Paez, F. B. M. van Zon, and Y. Iwasawa, Eds.), Vol. 2, p. 257. World Scientific, London, 1996.
49. Ankudinov, A. L., Ravel, B., Rehr, J. J., and Conradson, S. D., *Phys. Rev. B* **58**, 7565 (1998).